Burner Rig Hot Corrosion of Five Ni-Base Alloys Including Mar-M247

J.A. Nesbitt
NASA Glenn Research Center
Cleveland, OH 44135

K. Harris
Cannon-Muskegon Corporation
Muskegon, MI 49443

R. Helmink
Rolls-Royce
Indianapolis, IN 46206

G. Erickson (retired)
Cannon-Muskegon Corporation
Muskegon, MI 49443

ABSTRACT

The hot corrosion resistance of four new Ni-base superalloys was compared to that of Mar-M247 by testing in a Mach 0.3 burner rig at 900°C for 300 1-hr cycles. While the Al content was held the same as in the Mar-M247, the Cr and Co levels in the four new alloys were decreased while other strengthening elements (Re, Ta) were increased. Surprisingly, despite their lower Cr and Co contents, the hot corrosion behavior of all four new alloys was superior to that of the Mar-M247 alloy. The Mar-M247 alloy began to lose weight almost immediately whereas the other four alloys appeared to undergo an incubation period of 50-150 1-hr cycles. Examination of the cross-sectional microstructures showed regions of rampant corrosion attack (propagation stage) in all five alloys after 300 1-hr cycles . This rampant corrosion morphology was similar for each of the alloys with Ni and Cr sulfides located in an inner subscale region. The morphology of the attack suggests a classic "Type I", or high temperature, hot corrosion attack.

INTRODUCTION

Hot corrosion of metals and superalloys has been studied extensively over the past 30 years. Much work has been performed dealing with salt deposition, deposit chemistry, gas thermodynamics, and possible mechanisms, and many excellent reviews have been written.[1-6] In order to gain this understanding, careful studies have been done in controlled environments with pure metals or simple alloys. Often the gas environment is controlled to yield a fixed SO_2-SO_3 partial pressure and a deposit of known composition (most commonly Na_2SO_4) is deposited on the surface. In contrast, the burner rig, with a rotating carousel, is an excellent tool for comparing the corrosion resistance of different alloys under identical, although less controlled, conditions. In a burner rig, most of the parameters of known importance are less well defined. Predictions can be made concerning the composition of the

gas environment, but not easily measured, and although the salt flow into the burner can easily be controlled, the salt chemistry and rate being deposited on a sample is not readily known.

Most burner rig hot corrosion studies have involved deposition of a liquid sulfate on the surface of the test samples. The sulfate, most commonly Na_2SO_4, may be directly injected into the burner, or a Na-containing salt can be injected. In this latter case, S in the fuel combines with the salt to produce Na_2SO_4 in the burner. For a liquid sulfate to be deposited, the sample temperature must be above the melting point of the sulfate but below the dew point. Within this environmental window, the molten sulfate can condense and remain molten on the sample surface. The melting point for $NaSO_4$ is known to be 884°C. Calculations have been made to predict the dew point for Na_2SO_4 deposition in burner rigs as a function of pressure, Na concentration and different S contents in the fuel.[7] However, synthetic sea salt is often used in burner rig studies to more closely simulate the environment of an aero engine operating near coastal waters. Sea salt consists of mixed chloride salts containing Na, Mg, Ca and K as well as nearly 10% Na_2SO_4. The ternary phase diagram for the sulfates of Na, Mg and Ca indicates several eutectic troughs leading to a ternary eutectic point at only 650°C.[2] Deposition studies of synthetic sea salt injected into a Mach 0.3 burner rig operated at 900°C showed that Na, Mg, Ca, K and SO_4 were deposited on a Pt target.[8] The absence of Cl indicated that all of the salt was converted to sulfate in the burner. In addition, the burner rig also deposited small quantities of Fe, Ni, Cr, Si and Mn from corrosion/erosion of the burner and nozzle.[8] Hence, use of synthetic sea salt with burner rig testing can produce molten sulfate deposits, although the exact composition of the melt may be uncertain.

A study was recently completed to examine new alloys and casting processes for an integrally bladed turbine wheel in the Rolls-Royce Model 250 engine. This work was a collaborative effort involving industrial, academic, and government partners. The Ni-base superalloy, Mar-M247, was selected as the baseline material for this alloy development program. Results summarizing the mechanical properties and casting processes have recently been reported.[9] The present paper will discuss the burner rig testing which was undertaken to evaluate the hot corrosion behavior of the baseline and the four new alloys examined in this program.

EXPERIMENTAL

As stated above, Mar-M247 was selected as the baseline material for the alloy development program.[9] The hot corrosion behavior of this baseline and four new alloys was examined. Two alloys were compositional variants of the superalloy designated CM 186 LC,* while two additional alloys were compositional variants of the superalloy CMSX-10.* The alloy designations and compositions of the five alloys examined in this study are shown in Table 1. It should be noted that the compositions of the four new alloys were chosen to optimize mechanical strength and castability, not specifically corrosion behavior.

Samples were EDM wire cut from polycrystalline castings into a pin geometry with dimensions 0.6 cm (0.25 in) diameter by 7 cm (2.75 in) length. The surface of each of the pins was polished through 600 grit SiC paper. The samples were tested by repeated cycling in and out of the flame of a burner rig. The burner operated with Jet A fuel to produce an exhaust gas velocity of Mach 0.3 at atmospheric pressure. A synthetic sea salt solution† was injected into the burner combustor to yield a 2

* Trade name

† Synthetic sea salt consists primarily (>99%) of $58.5NaCl\text{-}26.5MgCl_2\cdot6H_2O\text{-}9.7Na_2SO_4\text{-}2.8CaCl_2\text{-}1.6KCl$ wt%.

ppmw salt loading in the hot combustion exhaust air. The samples were held in a 15 sample carousel with approximately 5 cm (2 in) of each sample exposed above the carousel platform. The carousel, which was rotated at approximately 300 RPM, was cycled automatically from the heating position to the cooling position. In the heating position, the hot gas stream impingement was centered on the exposed sample length. During cooling, the samples were blasted with ambient room temperature air. For each cycle, the carousel was held in the heating position for 60 minutes and the cooling position for a minimum of 6 minutes.

The burner was operated to yield sample temperatures of approximately 1650°F (900°C). This temperature was controlled by a 2-color pyrometer continuously monitoring the rotating samples and adjusting the fuel-to-air ratio to maintain the desired temperature. The sample temperatures were also continuously monitored and recorded by a laser pyrometer. Thermocoupled dummy samples verified the accuracy of the pyrometer temperature measurement to approximately ± 8°C (15°F). Although the laser pyrometer showed a higher temperature than that for the two color pyrometer and thermocouples, the temperature profile measured with this pyrometer indicated that sample heating to the test temperature and cooling to ambient air temperature occurred within a couple of minutes (Figure 1). Two samples of each alloy were tested in the carousel. Samples were removed from the carousel and weighed every ten cycles. Samples were randomly placed back in the same carousel location after weighing, i.e., no specific angular orientation of the individual pins was maintained during testing. Further details regarding the burner rig is given elsewhere.[8]

Weight Change

The weight change data clearly shows that the hot corrosion resistance of the new alloys is superior to that of the Mar-M247 alloy. Figure 2a shows that the Mar-M247 alloy began losing weight almost immediately. This rapid weight loss is due to accelerated scale formation and spalling, and, as will be shown below, resulted in a visible reduction in the diameter of the sample. The four new alloys appeared to undergo a more typical incubation period with low weight gains (sometimes referred to as initiation) followed by a propagation stage with higher rates of weight gain. Alloys A, B and C appeared to undergo this incubation period with low weight gains for approximately 150 1-hr cycles, whereas Alloy D exhibited a shorter incubation period of approximately 50 cycles (Figure 2b). For Alloy D, the rate of weight change continued at a higher rate between 50 and 250 cycles. Between 250 and 300 cycles, at least one sample of each of the four new alloys experienced a much higher rate of weight gain (propagation stage) through the end of the test (300 cycles). One sample of Alloy D exhibited a significant weight loss during the last 200 cycles due to spalling of the reaction product. As will be shown below, the attack on the samples was not uniform around the circumference of the sample so that ranking the alloys according to weight gain alone, except for the obviously poor behavior of the Mar-M247 alloy, could be misleading.

Sample Morphology

The region of maximum attack on most of the pins was located 3.2 cm (1¼ in) from the top except for Alloy C where the visibly-attacked region appeared to be approximately 0.6 cm (¼ in) lower (Figure 3). As stated above, the reduction in the sample diameter in the Mar-M247 samples is clearly visible. Most of the corrosion attack on the four new alloys caused the samples to swell. Large cracks were often associated with these swollen regions and occasionally large pieces were observed to have spalled at these locations.

Sample Microstructures

Composite Photos. The samples were copper plated in an attempt to keep the fragile surface scale and reaction products intact. Each sample was then sectioned through their region of maximum

attack at 3.2 cm (1¼ in) from the top (3.8 cm for Alloy C). Composite figures of these regions were produced to show the nonuniform attack and the total reduction in cross-sectional area. Cross sections for two of the alloys are shown in Figure 4. The circle on each figure indicates the original sample diameter (~0.64 cm, 0.25 in) which was determined from a composite figure of an unattacked region of the sample located below the carousel platform. It is apparent from these figures that the corrosion attack was not uniform around the circumference of the sample. The cross-sectional area of metal remaining after testing (area A in Figure 4b) was measured by image analysis. The relative extent of attack for each alloy was then determined by calculating the reduction in cross-sectional area (A/Ao), where Ao is the original cross-sectional area of the sample (indicated as the circles in Figure 4). These values for A/Ao are shown in Table 2. It is interesting to note that the reduction in cross-sectional area is not directly related to weight gain due to the localized, nonuniform attack. For instance, the Alloys A and C gained approximately the same weight after 300 cycles. However, the reduction in area is 0.68 and 0.80 respectively. Where a portion of the sample appeared to have undergone little internal attack, (i.e., left side of sample in Figure 4b), the center of the sample could be defined and a maximum attack penetration measured (see short arrow in Figure 4b). For the Mar-M247 and Alloy D samples, the attack had encompassed the entire sample circumference and only an average penetration distance was calculated. The average and maximum penetration distances are also shown in Table 2.

SEM Photos. All alloys showed some regions of rampant attack which has also been referred to as the propagation stage.[1,10] However, Alloys A, B and C showed some regions on the surface still in the initiation, or incubation stage. Consequently, the corrosion morphologies will be discussed in terms of this progression from initiation, to intermediate, through rampant attack. Energy dispersive analysis (EDS) was used extensively to identify the oxides and sulfides.

Initiation. In Alloys B and C, a multilayer oxide scale was commonly observed in regions with no significant subscale attack (Figure 5a). The outer oxide layer ("A" in Figure 5a) was Ta and Ni rich and is likely a transient oxide which first forms on the surface. The second layer ("B") was primarily Al, presumably alumina. Ca and Mg from the sea salt were detected in both layers. An alumina layer ("C"), without Ca and Mg, could be observed at the innermost region of the scale. Below the alumina layers, small Cr sulfides were observed separated from the oxide by a layer of metal without oxides or sulfides. In Alloy A, which contains less Ta, only a single oxide layer rich in Al and Ta was observed on the surface although Mg, Ca and S were also detected in this layer (Figure 5b). Large Cr sulfides were evident in the alloy and at the scale/metal interface.

The chemical conditions or microstructures which initiate or trigger the rampant attack are not clear. Two possible sites showing oxide formation below the outer layers are shown in Figure 6. In Figure 6a, an Al and Ta mixed oxide formation ("A") is growing below an outer, primarily alumina layer ("B"). The inwardly-growing mixed oxide is surrounded by Cr sulfides. In Figure 6b, the outer Al and Ta scale ("C") has incorporated regions of unoxidized Ni-, Co-, and W-rich metal ("F") as well as regions of mixed oxides ("D") containing Al, Ta, Ca, Ti, Cr and Ni. Interestingly, below these regions is a dark oxide ("E") consisting almost entirely of Al and O, presumably alumina. The detection of Ca and Mg within these and similar subscale regions indicates the presence of the corrosive reactants within these regions.

Intermediate Attack. Larger regions of internal attack, designated as intermediate attack, are shown in Figure 7. This level of attack shows inwardly growing oxides, primarily Al and Ta, trapping islands of metal within the subscale region. The metal islands are almost always depleted of the oxygen active elements Al, Ta, Cr, Hf, and Ti. As expected, Al and Hf oxides appear to be the first

oxides to form at the innermost regions of the attacked zone. Cr sulfides were always present below the attacked region.

Rampant Attack. At the edges of the rampant attack regions, large Cr sulfides were always observed, as shown in the typical microstructure in Figure 8. Many of the sulfide stringers appear connected with hollow channels (dark regions in Figure 8b,c). Magnified views, with EDS analysis showed that many of these dark hollow regions had alumina shells. Most of the large sulfides showed only the presence of Cr and S. However, some Ni sulfides were observed near the edges of the rampant attack where the Cr sulfides were numerous (Figure 8c).

Magnified views of the regions of rampant attack show a subscale zone consisting of both oxides and metal. The two samples which showed a rampant attack morphology around the entire sample circumference are shown in Figure 9. Figure 9c shows that the outer 100 microns of the subscale at this location on the Mar-M247 alloy was totally oxidized. Fracture and spallation of this brittle oxidized layer on cooling likely accounts for the large weight loss and overall reduction in the sample diameter of this sample (see Figure 3). EDS of the oxides throughout the subscale indicate high concentrations of Al as well as the refractory components Ta, Hf, and W. The unoxidized metal remaining in the subscale was primarily Ni and Co. The inner region of the scale showed the presence of many smooth, oval Cr sulfides, smooth alumina stringers and distinct regions of mixed refractory oxides (Figure 10). These smooth alumina stringers often appeared to follow grain boundaries and gave the appearance of a molten attack (Figure 10a). As mentioned previously, the structure of many of the stringers was that of an alumina shell with a hollow core. Cr sulfides were occasionally observed within the subscale but were most abundant in this innermost region of the subscale. It appears that oxidation depleted the Al and refractory elements from the Ni and Co islands remaining in the subscale, however, Cr may have been depleted by both oxidation and sulfide formation. Ni sulfides were also occasionally observed at the inner region of the subscale undergoing rampant attack.

DISCUSSION

It is clear that the four new alloys exhibit improved corrosion resistance over that of the Mar-M247 alloy. This is especially surprising since the Mar-M247 alloy contains more Cr (8.4% vs. 2.7-5.9%) than the other four alloys (see Table 1), an element known to be beneficial for hot corrosion resistance.[1] However, burner rig hot corrosion testing of numerous superalloys under similar test conditions (900°C) showed that Cr contents of 12% or more were generally much more resistant than alloys with less than 10%.[11] Hence, the Cr content, when less than 10%, may not alone be a significant determinant of the hot corrosion behavior. Since there are only small differences in the Al (5.5-5.7%) and Hf (1.2-1.6%) contents between Mar-M247 and the other alloys, the difference in the behavior must be sought elsewhere. The Mar-M247 alloy contains the lowest Ta level, an element which is generally considered to be beneficial in hot corrosion resistance.[1] However, Mar-M247 contains 3% Ta compared to only 3.3% in Alloy A. In contrast, Mo and W are considered detrimental and have been linked with changing the sulfate melt from basic to acidic fluxing conditions.[1,12,13] The Mar-M247 alloy contains the highest Mo content, but only 0.7% vs. 0.5% for several of the other alloys. Likewise, the W level in Mar-M247 is also greater than that in the other four alloys, but only 10% vs. 8.5% in Alloys A and B. Ti has been observed to be detrimental to the hot corrosion behavior of NiAl,[8] but Mar-M247 has only 1% Ti vs. 0.75% in Alloy A. The only element present in the four new alloys (3-6%) but absent in Mar-M247 is Re. There is limited evidence that Re is beneficial to the hot corrosion resistance.[14] In the present limited study, it is impossible to positively identify the positive or negative contributions of individual constituents in the alloys. It is likely that the better

behavior of the four alloys is not due to a single element, but rather to a combination of elements having a synergistic effect.[11,15,16] Based on the weight change data (Figure 2), it appears that the benefit could be in delaying the onset of the rampant attack (i.e., extending the incubation period). It appears noteworthy that the rampant corrosion morphology for all five alloys is very similar.

In regard to differences between the four new alloys, only the weight change of Alloy D (Figure 2b) indicated a quicker initiation of the hot corrosion attack. However, a comparison of the reduction in areas (Table 2) indicates that Alloys C and D experienced similar amounts of attack (A/Ao= 0.8 vs.0.78, respectively). Similarly, there is little difference reflected in the weight change between Alloys A and B (Figure 2b) although the reduction in area indicates significantly more attack on the former than the latter alloy (A/Ao=0.68 vs. 0.82, respectively). Hence, there is some difficulty in correlating the weight gains with the measured reductions in area. Consequently, as stated above, it is impossible to relate the compositional differences between the four bars to differences in their corrosion behavior.

It appears that the initial oxide scale on the four new alloys is Al and Ta rich. However, the appearance of sulfides in the alloy indicates that S penetrates the outer scale. Based on earlier deposition studies[8] at 900°C, it can be assumed that injection of the synthetic sea salt into the burner produced a molten sulfate deposit on the surface of the test samples. Other studies suggest that at 900°C, the SO_2/SO_3 pressures in the burner rig operating at atmospheric pressure would likely result in a basic molten salt on the surface of the samples.[5] This molten salt could flux, or dissolve the Al/Ta scale allowing penetration of the S into the alloy. However, where W carbides exist at the surface, or in the Mar-M247 alloy with the higher W content, the W could change the molten salt chemistry to produce an acidic melt resulting in acidic fluxing conditions. It is also possible that the Al/Ta scale, after growing to a sufficient thickness, was breached by cracking due to the thermal cycling to room temperature. In any event, it is obvious that the outer scale is breached and the corrosion reactants gain entry to the alloy. It appears that once the outer scale is breached, Al and Ta are internally oxidized and a protective outer scale is never reformed.

The morphology of the attack, with the sulfides below the internal oxide subscale, suggests a classic "Type I", or high temperature, hot corrosion attack. This morphology is commonly observed in the hot corrosion attack of superalloys at temperatures above 800°C.[1,17,18] During the stage designated as intermediate attack, Al, Ta, and Hf continue to be oxidized largely depleting the base alloy of these elements. The oxidation reduces the oxygen concentration in the sulfate melts causing the melts to become more basic. The oxidation also frees S to penetrate the alloy forming the Cr sulfides below the internally oxidized subscale. The observation of Ca and Mg within this subscale region indicates the presence of these sulfates below the alloy surface.

As stated above, the chemical conditions or microstructures which initiate or trigger the rampant attack are not apparent. It is not known whether the high density of sulfides below the oxide subscale is a prerequisite to rampant attack, or a consequence of the rampant attack. The high density of sulfides was always observed at the edges of the rampant attack (Figure 8). The selective oxidation of Al from molten sulfates in channels in the subscale likely resulted in the formation of the hollow alumina stringers.

CONCLUSIONS

- The four new alloys show improved hot corrosion resistance over the Mar-M247 alloy.

- All five of the alloys showed some regions of rampant attack (i.e., propagation stage) on the surface.

ACKNOWLEDGEMENTS

This program was supported in part by the NASA Glenn Research Center under Cooperative Agreement NCC3-387.

REFERENCES

1. F.S. Pettit and C.S. Giggins, "Hot Corrosion" in *Superalloys II*, edited by C.T. Sims, N.S. Stoloff and W.C. Hagel, John Wiley & Sons, Inc., New York, NY, p. 327, 1987.

2. N.S. Bornstein, JOM, Nov. 37, 1996.

3. J. Stringer, MRS Int'l Mtg. On Adv. Mats., Vol. 4, 407, 1989.

4. G.H. Meier, Materials Science & Engineering, A120, 1, 1989.

5. J. Stringer, J. de Physique IV, Vol. 3, Dec, 43, 1993.

6. J. Stringer, Materials Sci. & Technol. Vol. 3, 482, 1987.

7. N.S. Jacobson, Ox. Met., Vol. 31, 91, 1989.

8. J.A. Nesbitt, "Hot Corrosion of Single-Crystal NiAl-X Alloys," NASA TM 113128, 1998.

9. R.C. Helmink, R.A. Testin, A.R. Price, R. Pachman, G.L. Erickson, K. Harris, J.A. Nesbitt and J.F. Radavich, "Advanced Superalloys and Tailored Microstructures for Integrally Cast Turbine Wheels," in *Superalloys 2000*, edited by T.M. Pollock, R.D. Kissinger, R.R. Bowman, K.A. Green, M. McLean, S.L. Olson and J.J. Schirra, TMS, Warrendale, PA, p. 171, 2000.

10. J. Stringer, D.P. Whittle and R.K. Hughes, Corros. Sci., Vol. 17, 529, 1977.

11. D.L. Deadmore, "Effect of Alloy Composition on Cyclic Flame Hot-Corrosion Superalloys at 900°C," NASA Technical Paper 2338, July 1984.

12. G.C. Fryburg, F.J. Kohl, C.A. Stearns and W.L. Fielder, J. Electrochem. Soc., Vol. 129, 571, 1982.

13. N. Birks, G.H. Meier and F.S. Pettit, JOM, Dec., 28, 1987.

14. M. Kawakami, A. Baba, C. Ikeda, N. Yukawa, M. Morinaga and K. Ito, MRS Int'l. Mtg. On Adv. Materials, Vol. 4, 431, 1989.

15. K. Matsugi, M. Kawakami, Y. Murata, M. Morinaga, N. Yukawa and T. Takayanagi, ISIJ, Vol. 78, 821, 1992.

16. K. Matsugi, Y. Murata, M. Morinaga, and N. Yukawa, ISIJ, Vol. 78, 158, 1992.

17. G.J. Tatlock and T.J. Hurd, Werkstoffe und Korrosion, Vol. 41, 710, 1990.

18. M Levy, R. Huie and F. Pettit, Corrosion, Vol. 45, 661, 1989.

Table 1.
Nominal compositions of the superalloys examined in this study (weight %).

Alloy Designation	Trade* Name	Cr	Co	Mo	W	Re	Nb	Ta	Al	Ti	Hf	C	B	Zr	Ni
Mar-M247	Mar-M247	8.4	10	0.65	10			3.1	5.5	1	1.4	0.16	0.015	0.05	Bal
	CM 186 LC‡	6	9	0.5	8	3		3	5.7	0.7	1.4	0.07	0.015	0.005	Bal
Alloy A**	CM 186 Mod	5.9	9.4	0.4	8.5	3		3.3	5.7	0.75	1.5	0.09	0.019	0.01	Bal
Alloy B**	CM 681	5.4	9.3	0.5	8.5	3		6.2	5.7	0.15	1.6	0.11	0.018	0.015	Bal
	CMSX-10‡	2	3	0.4	5	6	0.05	8	5.7	0.2	0.03				Bal
Alloy C†	CM 4670	4	3.4	0.5	5	5.3	0.05	8	5.7	0.13	1.2	0.09	0.017	0.015	Bal
Alloy D†	CM 4670C	2.7	3.2	0.4	5	6	0.05	8	5.7	0.08	1.2	0.05	0.02	0.025	Bal

* Trade name or alloy designation used in Reference 9.
** Alloys based on CM 186 LC.
† Alloys based on CMSX-10.
‡ Originating alloy shown for convenience.

Table 2
Reduction in Area and Penetration after 300 1-Hr Cycles

Alloy	Reduction in Area A/Ao*	Penetration, μm (mils) Average	Maximum
Mar-M247	0.46	1000 (40)	-
Alloy A	0.68	530 (21)	965 (38)
Alloy B	0.82	125 (5)	810 (32)
Alloy C	0.80	330 (13)	1170 (46)
Alloy D	0.78	355 (14)	-

* The nominal cross sectional area Ao, of each sample was 0.317 cm^2 (0.0491 in^2).

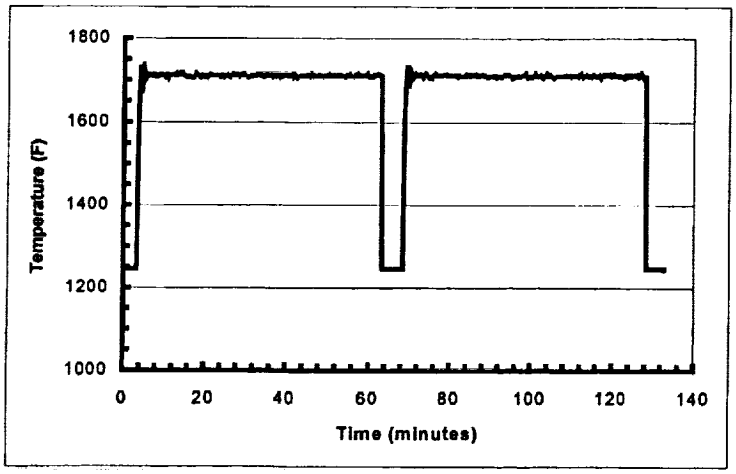

Figure 1 Temperature profile for the samples measured by the laser pyrometer. (The laser pyrometer does not operate below approximately 704 °C (1300°F)).

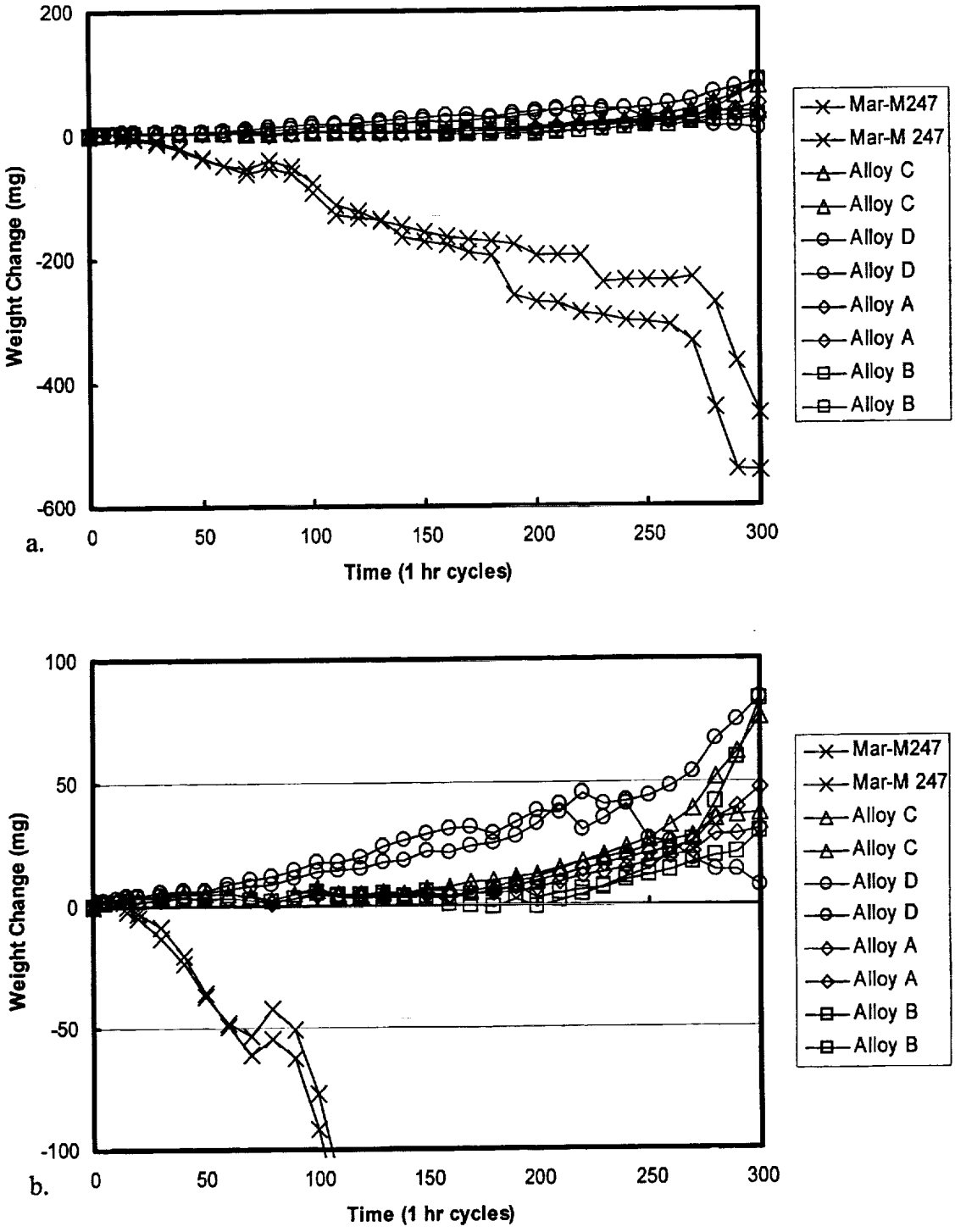

Figure 2. Weight change during hot corrosion testing (a) extended axis, (b) magnified axis.

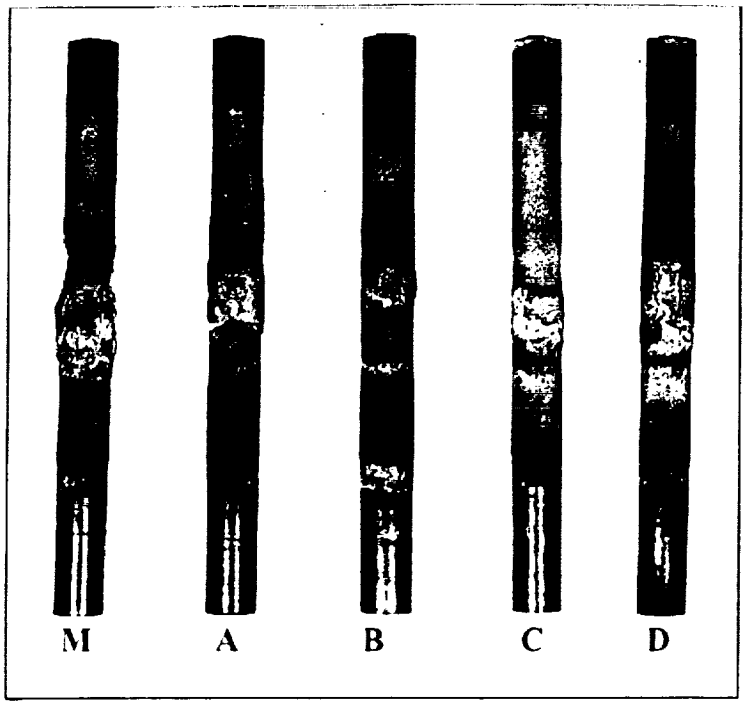

Figure 3. Macrophotographs of the samples after 300 1-hr cycles at 900°C (M:Mar-M 247)

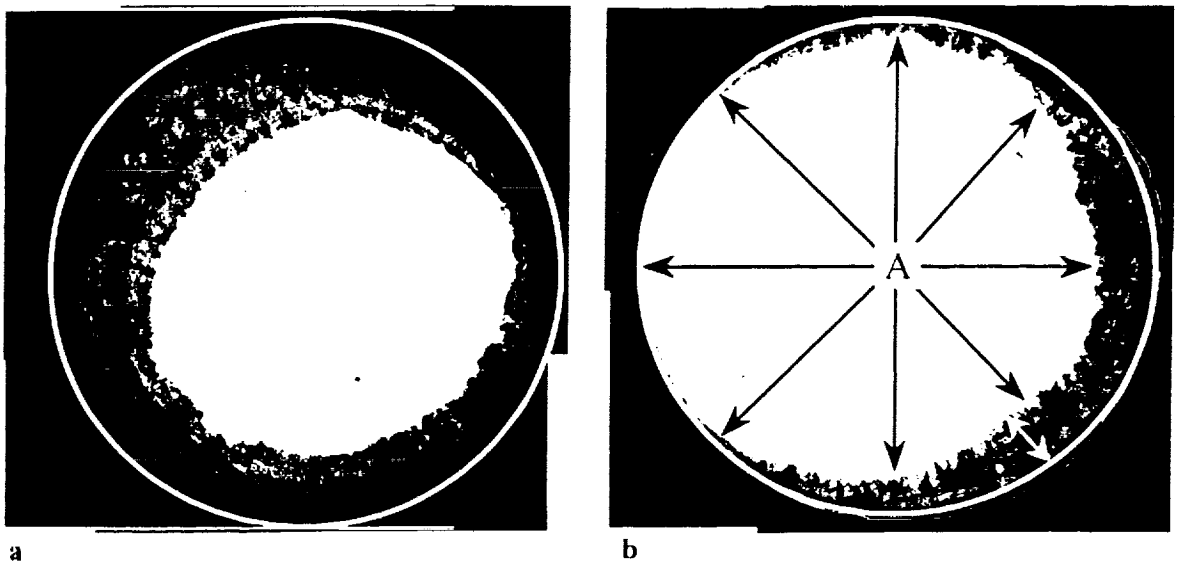

Figure 4. Cross sections of two of the samples at the region of maximum attack, (a) Mar-M247, (b) Alloy B. The black arrows in b. indicate the cross-sectional area "A". The smaller white arrow at 5 O'clock indicates the location of the maximum penetration.

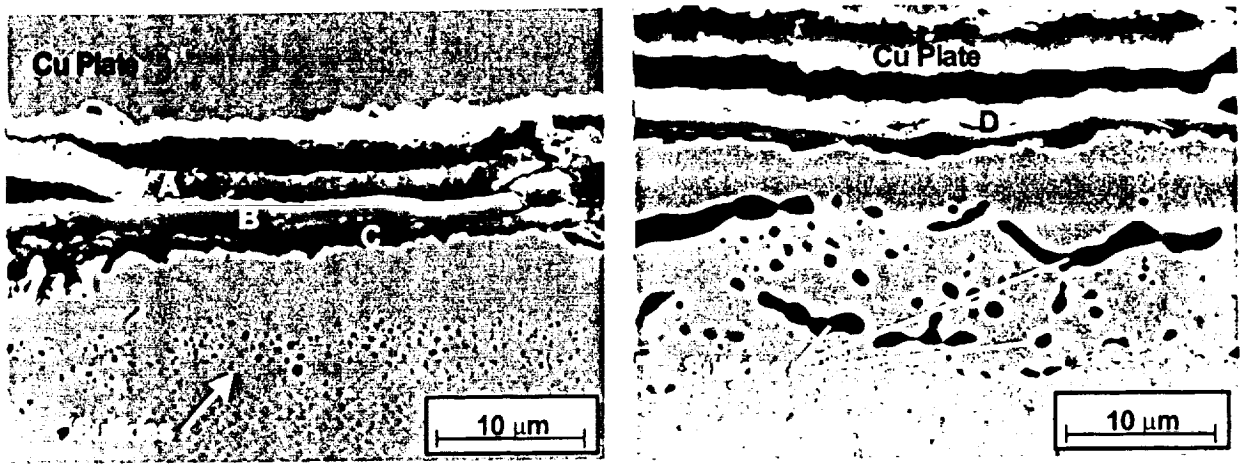

a. b.

Figure 5. SEM image of the scale prior to internal oxide formation on (a) Alloy B and (b) Alloy A. The outer scale "A" is Ta and Ni rich while the center layer "B" contains primarily Al. Both layers A and B contain some Ca and Mg from the sea salt. The inner layer "C" contains primarily Al without Ca or Mg. "D" is primarily Al with significant amounts of Ta and also contained Mg, Ca and S. Cr sulfides were also detected at the scale/metal interface below "D".

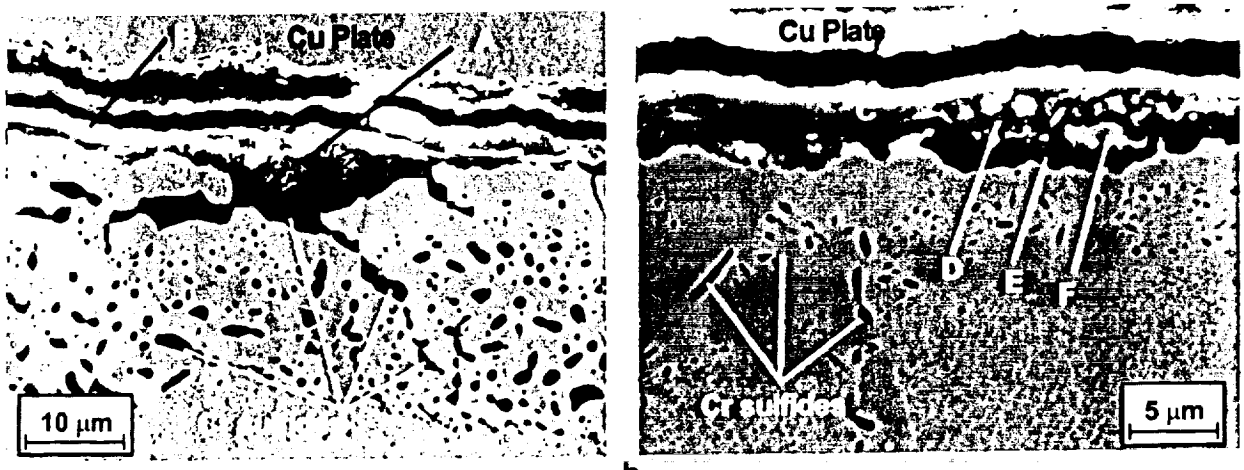

a. b.

Figure 6. Possible sites for the initiation of subscale oxide growth on (a) Alloy A and (b) Alloy B. "A" is a growth of Al- and Ta-rich oxide with measurable amounts of Ca, Ti, Cr Ni and Hf. "B" is the outer oxide scale, consisting primarily of Al with small concentrations of Mg, Ta, Cr and Ni. Numerous Cr sulfides are evident in the alloy. "C" is the typical Al and Ta outer oxide layer without measurable quantities of Ca. "D" is mixed oxides of Al, Ta, Ca, Ti Cr and Ni. The dark oxide at the bottom of the attacked region, "E", consists almost entirely of Al and O. "F" is a metal island of Ni, Co and W.

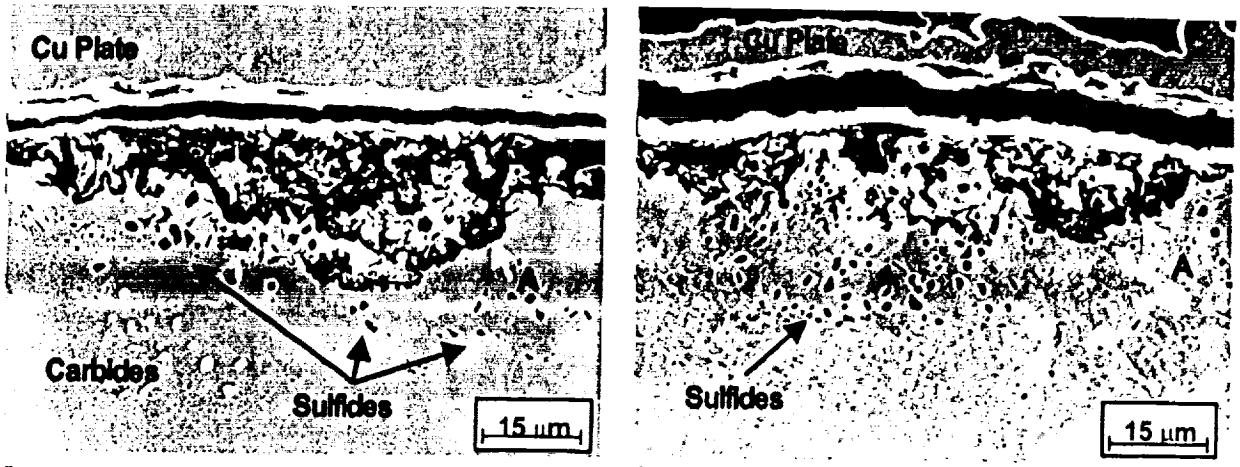

a. b.

Figure 7. Intermediate subscale attack on the surface of (a) Alloy B and (b) Alloy C. The arrows at "A" points to Al-rich oxides (dark) which were common at the inner reaches of the attack zone. Unoxidized metal depleted in Al, Ta, and Cr was always present in the attacked region.

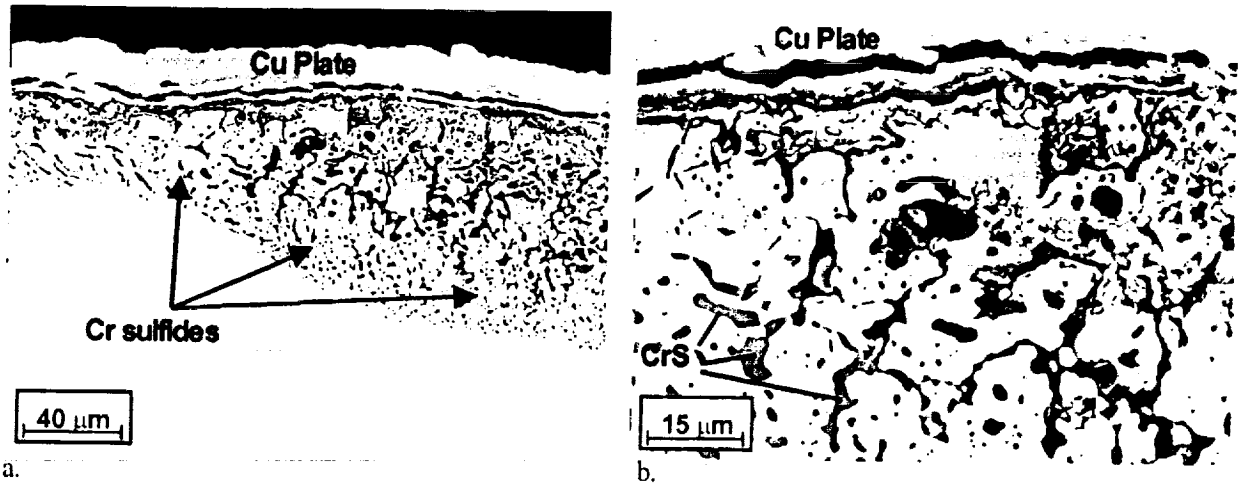

a. b.

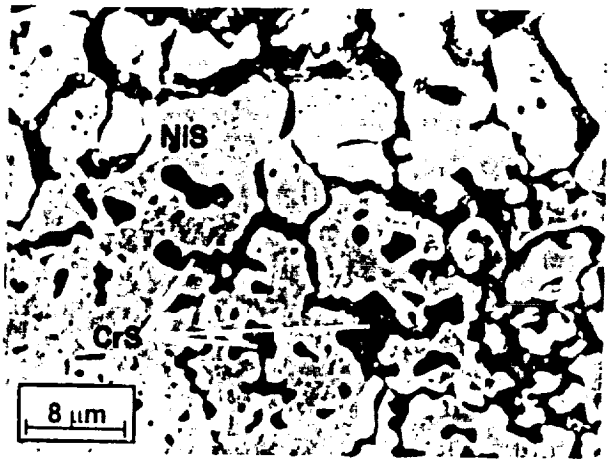

c.

Figure 8. Edge of the rampant attack region on the (a,b) Alloy B and (c) Alloy C. Large sulfides were always present at the edge of rampant attack. "CrS" indicates Cr sulfides, "NiS" indicates a Ni sulfide. The dark regions are often hollow with alumina shells.

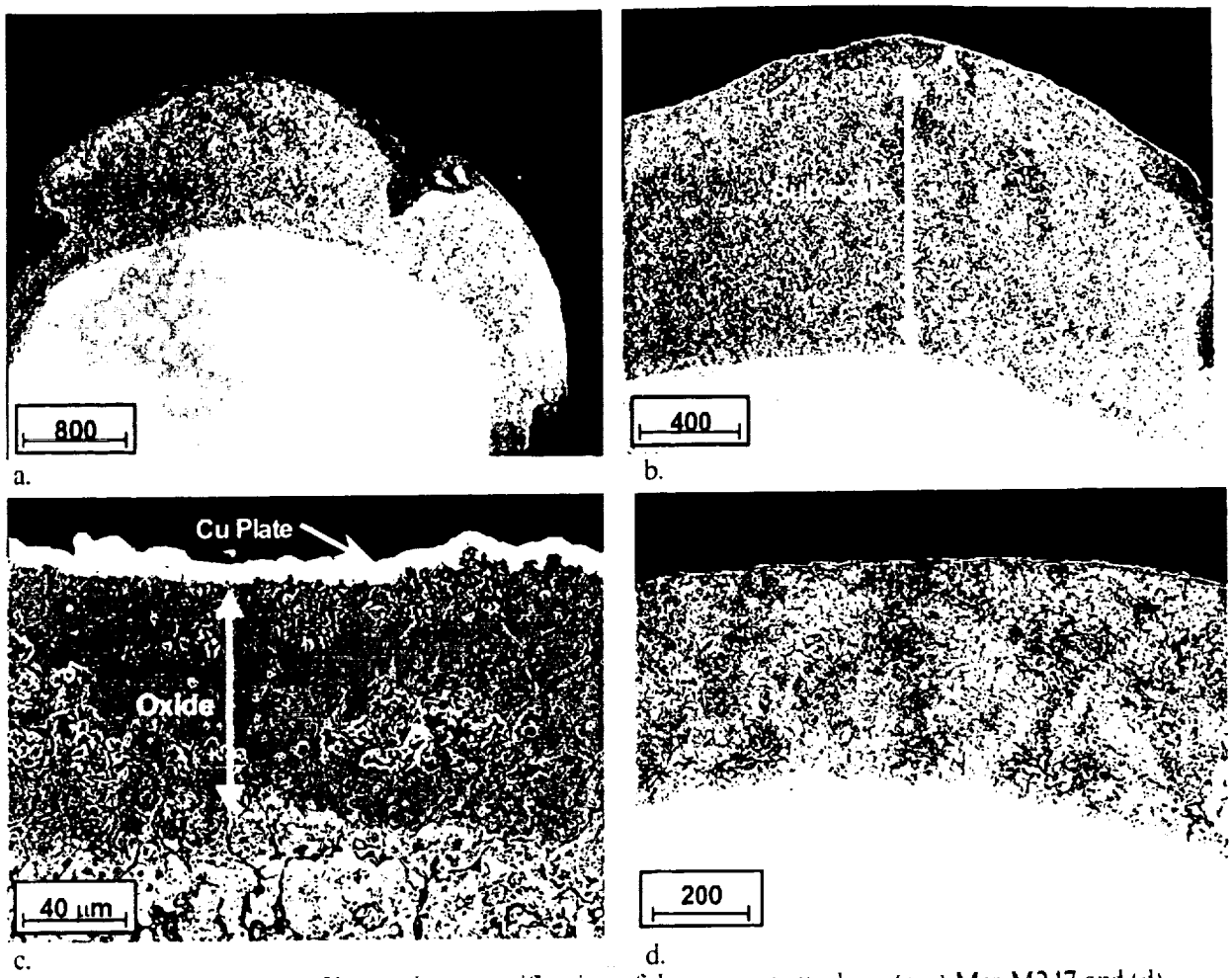

Figure 9. SEM images of increasing magnification of the rampant attack on (a-c) Mar-M247 and (d) Alloy D. Image in (c) shows the completely oxidized outer region of the subscale ("A" in image (b)).

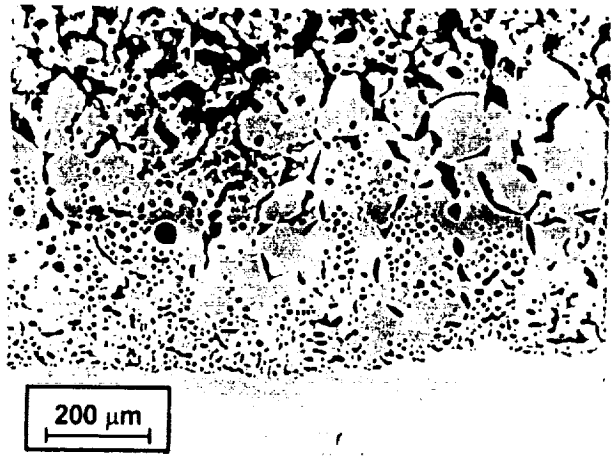

a.

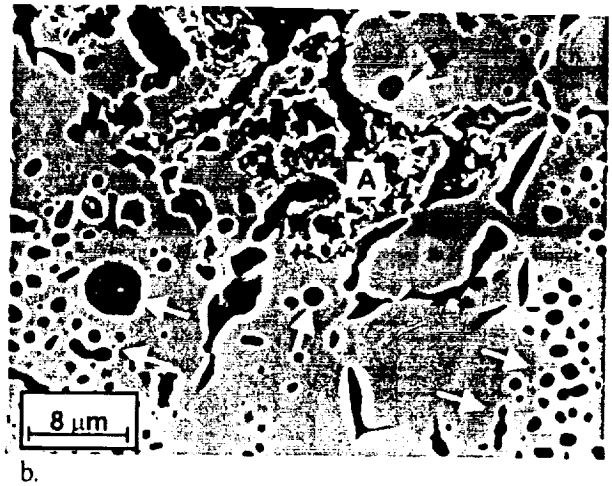

b.

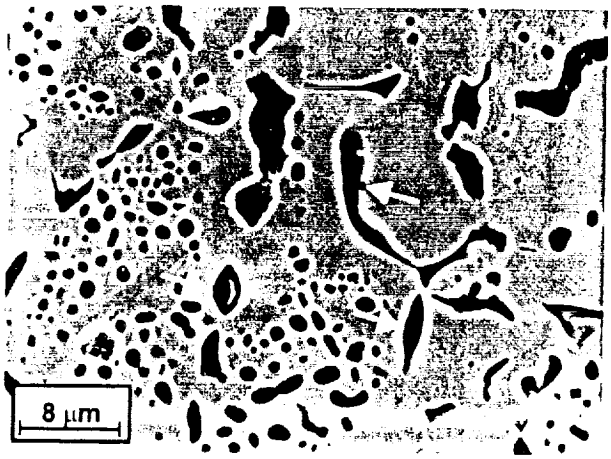

c.

Figure 10. SEM images of the inner region of the subscale shown in Figure 9a-c. Area "A" in (b) consists of refractory oxides, primarily Ta and W. The arrows in (b) indicate Cr sulfides. The arrows in (c) indicate hollow oxide (alumina) stringers.